crystals

MDPI

Article

A Cost-Effective Long-Wave Infrared Detector Material Based on Graphene@$PtSe_2$/$HfSe_2$ Bidirectional Heterostructure: A First-Principles Study

Jianzhi Zhang [1], Hongfu Huang [1], Junhao Peng [1], Chuyu Li [1], Huafeng Dong [1,2,*], Sifan Kong [3], Yiyuan Xie [4], Runqian Wu [5], Minru Wen [1] and Fugen Wu [2,6]

1 School of Physics and Optoelectronic Engineering, Guangdong University of Technology, Guangzhou 510006, China
2 Guangdong Provincial Key Laboratory of Information Photonics Technology, Guangdong University of Technology, Guangzhou 510006, China
3 School of Software, South China Normal University, Foshan 528225, China
4 Hunan Provincial Key Laboratory of Grids Operation and Control on Multi-Power Sources Area, Shaoyang University, Shaoyang 422000, China
5 Guangdong Experimental High School, Guangzhou 510006, China
6 School of Materials and Energy, Guangdong University of Technology, Guangzhou 510006, China
* Correspondence: hfdong@gdut.edu.cn

Abstract: The Graphene@$PtSe_2$ heterostructure is an excellent long-wave infrared detection material. However, the expensive cost of $PtSe_2$ prevents its widespread use in infrared detection. In this paper, Hf was used to partially replace Pt to form Graphene@$(PtSe_2)_n(HfSe_2)_{4-n}$ (n = 1, 2, and 3) bidirectional heterostructures consisting of graphene and lateral $PtSe_2$/$HfSe_2$ composites based on first-principles calculations. Then, the new bidirectional heterostructures were compared with heterostructures formed by graphene with pure MSe_2 (M = Pt, Hf). It was found that the band gaps of the bidirectional heterostructures were between those of Graphene@$PtSe_2$ and Graphene@$HfSe_2$. Among these heterostructures, the Graphene@$(PtSe_2)_3(HfSe_2)_1$ bidirectional heterostructure has almost the same optical absorption properties in the infrared wavelength region of 1.33~40 μm as the Graphene@$PtSe_2$ heterostructure, and it improves the absorption in the near-infrared wavelength region of 0.75~1.33 μm. Such a designment may bring the material costs down (since $PtSe_2$ costs approximately five times more than $HfSe_2$). This study on the designment of the bidirectional Graphene@$(PtSe_2)_3(HfSe_2)_1$ heterostructure also illustrates a cost-effective design method for Pt-based IR detectors.

Keywords: long-wave infrared detector material; bidirectional heterostructure; optical absorption properties; first principles

Citation: Zhang, J.; Huang, H.; Peng, J.; Li, C.; Dong, H.; Kong, S.; Xie, Y.; Wu, R.; Wen, M.; Wu, F. A Cost-Effective Long-Wave Infrared Detector Material Based on Graphene@$PtSe_2$/$HfSe_2$ Bidirectional Heterostructure: A First-Principles Study. *Crystals* **2022**, *12*, 1244. https://doi.org/10.3390/cryst12091244

Academic Editors: Younghyun Kim, Sanghyeon Kim and Andreas Thissen

Received: 28 July 2022
Accepted: 31 August 2022
Published: 2 September 2022

1. Introduction

Transition metal dihalides (TMDs) have been investigated intensely in recent years, due to their fascinating electrical [1,2], mechanical [3], and optical characteristics [4,5]. They could provide the basic building blocks for a new generation of nanoelectronic devices based on 2D van der Waals (vdW) crystals [6,7]. Motivated by their prominent properties, numerous studies have been focused on the research of vdW heterostructures, such as $PtSe_2$/GaAs [8], MoS_2/WSe_2 [9], graphene/MoS_2 [10], and WSe_2/$HfSe_2$ [11]. It is widely demonstrated that constructing hybrid heterostructures is a potential way to fabricate nanoelectronic and optoelectronic devices with excellent performance [12,13].

Notably, $PtSe_2$ is an attractive material for broadband mid-infrared detectors due to its relatively high carrier mobility, superior ambient stability, and narrow-band structure [14,15]. Since it was discovered in 2004 [16], graphene has been widely used in a large variety of fields, owing to its mechanical as well as optical properties and high conductivity [17–25].

There are two components to graphene's low energy conductivity: intraband and interband contributions [26,27]. According to the zero gap of graphene, which limits its development and applications, Luo et al. [28] proposed that, by creating a Gr@$PtSe_2$ van der Waals heterostructure, the zero band gap of graphene could be opened, thus further expanding its response range. Later, Long et al. [29] experimentally corroborated Luo et al.'s proposal. They found that Gr@$PtSe_2$ shows a strong optical response (300 mA/W) at long wavelengths of 10.6 μm, indicating that it is a highly competitive candidate for long-wavelength infrared detectors. However, the high cost of $PtSe_2$ prevents its widespread use in photodetectors [30,31]. Is there a method to lower the cost without compromising performance? Doping is an effective method [32,33]. It has been reported that $HfSe_2$, with the same structure as $PtSe_2$, has greater carrier mobility, good optical sensitivity, and a low cost [34,35]. Similar to $PtSe_2$, $HfSe_2$ can also open the band gap of graphene [36]. Despite the fact that Zr and Hf have almost similar properties [37], Hf has better infrared light absorption properties (Figures S1 and S2). Therefore, we propose partially replacing Pt with Hf in order to reduce the cost of Gr@$PtSe_2$ materials.

Based on first-principles calculations, we investigated the structural, electrical, and optical properties of bidirectional heterostructures composed of graphene and lateral $PtSe_2/HfSe_2$ composites. We considered three cases with Hf doping ratios (Hf replacing Pt) of 75%, 50%, and 25% for $(PtSe_2)_n(HfSe_2)_{4-n}$ (n = 1, 2, and 3), and the bidirectional heterostructures were Graphene@$(PtSe_2)_n(HfSe_2)_{4-n}$ (n = 1, 2, and 3), abbreviated below as Pt_nHf_{4-n} and Gr@Pt_nHf_{4-n}, respectively. For comparison purposes, the results of heterostructure simulations for the production of graphene and pure $PtSe_2$ or $HfSe_2$ monolayers were also considered. We discovered that a bidirectional Gr@Pt_3Hf_1 heterostructure constituted of a partial (25%) substitution of Pt with Hf is an effective method of reducing material costs.

2. Computational Methods

The calculations were carried out utilizing a first-principles framework with a plane-wave basis set, as implemented in the Vienna Ab initio Simulation Package (VASP) code (VASP.5.4.4, Dr. Georg Kresse, Vienna, Austria) [38,39] and based on density functional theory under the generalized gradient approximation (GGA) with the Perdew–Burke–Ernzerhof (PBE) exchange–correlation functional [40]. Grimme's van der Waals correction (DFT-D3 with pair approximation [41]), which could offer a fair description of long-range vdW interactions, has been used in order to accurately characterize weak van der Waals interactions [42]. To prevent artificial interactions between periodic pictures, the z-direction vacuum space is adjusted to 25 Å. The kinetic energy cutoff for the plane waves is set at 520 eV. Brillouin zone integration is performed using $3 \times 4 \times 1$ Monkhorst–Pack k-grids for structure optimization and energy calculation, while $4 \times 7 \times 1$ Monkhorst–Pack k-grids are used for the calculation of optical properties. The geometric structures are completely relaxed until the energy and forces are converged to 10^{-6} eV and 0.01 eV/Å, respectively.

The optical propagation across a material is described using the dielectric function and the absorption coefficient [43–45]. The formula is as follows:

$$\varepsilon(\omega) = \varepsilon_1(\omega) + i\varepsilon_2(\omega) \quad (1)$$

The dielectric function, ε, is composed of two components: the real portion, ε_1, and the imaginary part, ε_2. The real component denotes the material's ability to retain energy and is calculated using the Kramers–Kronig formula:

$$\varepsilon_1(\omega) = 1 + \frac{2}{\pi} P \int_0^\infty \frac{\varepsilon_2^{\alpha\beta}(\omega')\omega'}{\omega'^2 - \omega^2 + i\eta} d\omega', \quad (2)$$

where P stands for the integral's primary value [46].

The loss factor is represented by the imaginary component, ε_2, in the following equation:

$$\varepsilon_2(\omega) = \frac{4\pi^2 e^2}{\Omega} \lim_{q \to 0} \sum_{c:v:k} 2\omega_k \delta(\epsilon_{ck} - \epsilon_{vk} - \omega) \times \left\langle u_{ck+e_\alpha q} \mid u_{vk} \right\rangle \left\langle u_{ck+e_\beta q} \mid u_{vk} \right\rangle^*, \quad (3)$$

where Ω represents the volume, α and β represent the Cartesian components, e_α and e_β represent the unit vectors, v and c represent matrix elements of the transition from the valence band state (u_{vk}) to the conduction band state (u_{ck}), and ε_{ck} and ε_{uk} represent the energies of the conduction and valence bands, respectively [46].

The absorption coefficient, $\alpha(\omega)$, is derived from the above two equations [46]:

$$\alpha(\omega) = \frac{\sqrt{2}\omega}{c} \left\{ \left[\varepsilon_1^2(\omega) + \varepsilon_2^2(\omega) \right]^{\frac{1}{2}} - \varepsilon_1(\omega) \right\}^{\frac{1}{2}} \quad (4)$$

3. Results

3.1. Geometrical Structures

The optimized lattice constants of graphene, 1T-$PtSe_2$, and 1T-$HfSe_2$ were 2.460 Å, 3.727 Å, and 3.752 Å, respectively, which are generally consistent with previous research [47,48]. The lattice mismatch of 0.66% for MSe_2 (M = Pt, Hf) demonstrates that the lattice mismatch of $PtSe_2$ and $HfSe_2$ was suitable for the construction of transverse heterojunctions using a monolayer of these two materials as substrates. To lessen the impact on the computations caused by the symmetry of the hexagonal phase structure, as seen in Figure S3, the hexagonal cell was transformed into a rectangular lattice cell. As shown in Figure 1, the long-edge lattice constants in the cut structure are represented by *a*, while the short-edge lattice constants are represented by *b*. The bidirectional Gr@Pt_nHf_{4-n} heterostructure was constructed using the most stable stacking technique [28]. To construct the Pt_nHf_{4-n} lateral heterostructures, we used a 2 × 2 supercell, and a 3 × 3 graphene monolayer was chosen to match the 2 × 2 Pt_nHf_{4-n} lateral heterostructures.

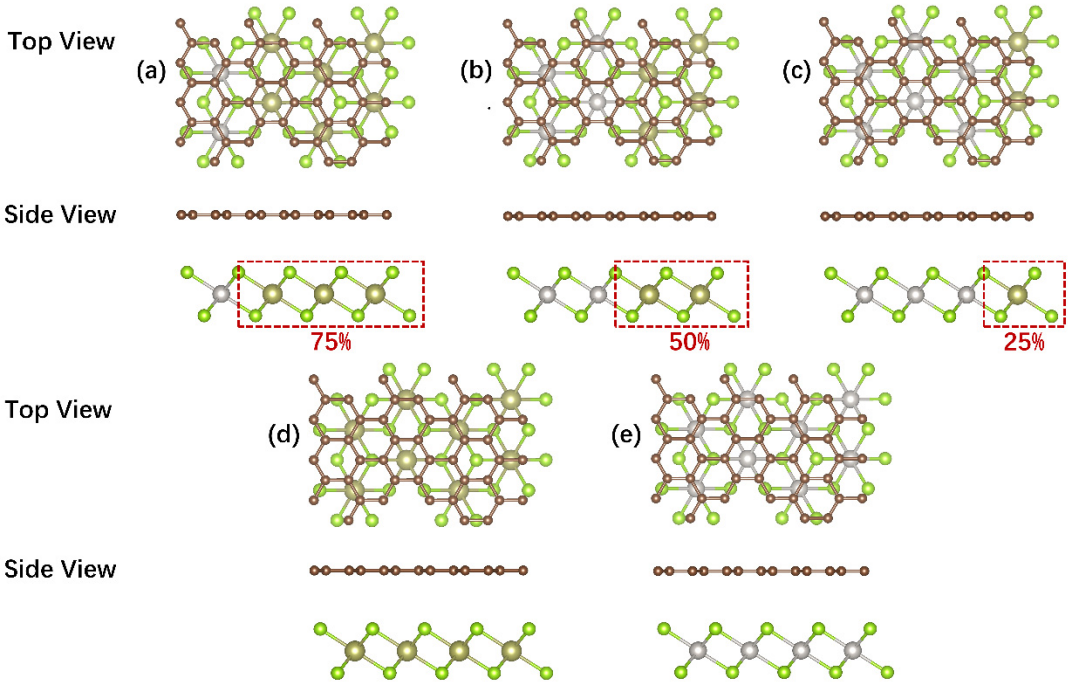

Figure 1. Top view and side view of stable configurations of (**a**) Gr@Pt_1Hf_3, (**b**) Gr@Pt_2Hf_2, (**c**) Gr@Pt_3Hf_1, (**d**) Gr@$HfSe_2$, and (**e**) Gr@$PtSe_2$. The brown, dark green, grey, and light green balls represent C, Hf, Pt, and Se atoms, respectively. The different partial (25%, 50%, and 75%) substitutions of bidirectional heterostructures are shown by the red, dashed-line square.

The stable structural information of Gr@Pt_nHf_{4-n} is shown in Table 1. As shown in Table 1, the bidirectional structure Gr@Pt_nHf_{4-n} had a stretched Pt–Se bond and a compressed Hf–Se bond compared to Gr@$PtSe_2$ and Gr@$HfSe_2$, resulting in decreased lattice constants for Gr@Pt_1Hf_3, Gr@Pt_2Hf_2, and Gr@Pt_3Hf_1. To quantitatively evaluate the interaction between the graphene and Pt_nHf_{4-n}, the interface binding energy (E_Δ) was also calculated according to the expression below:

$$E_\Delta = \left(E_{Gr@Pt_nHf_{4-n}} - E_{Pt_nHf_{4-n}} - E_{Gr}\right)/N_C, \quad (5)$$

where $E_{Gr@PtnHf4-n}$, $E_{PtnHf4-n}$, and E_{Gr} are the total energies of the bidirectional heterostructures of Gr@Pt_nHf_{4-n}, isolated lateral heterostructures of the Pt_nHf_{4-n} monolayer, and isolated graphene monolayer, respectively. N_C is the number of carbon atoms in the supercell. The binding energy per C atom, as a function of the interlayer distance (d) for Gr@Pt_nHf_{4-n}, Gr@$PtSe_2$, and Gr@$HfSe_2$, is plotted in Figure 2. As observed in Figure 2, $-E_\Delta$ is negative, indicating that the heterostructure arrangement between the graphene monolayer and the Pt_nHf_{4-n} substrate was stable, and the binding energy varied significantly as the interlayer distance between the graphene and Pt_nHf_{4-n} layers varied. The most stable interlayer distances for Gr@Pt_nHf_{4-n} varied between 3.3~3.5 Å, and Gr@Pt_3Hf_1 had lower binding energy than Gr@Pt_1Hf_3 and Gr@Pt_2Hf_2 for a given interlayer distance. In addition, when the structure was stable, the binding energy of Gr@Pt_3Hf_1 was lower than that of Gr@Pt_1Hf_3 and Gr@Pt_2Hf_2. Graphene adsorbed better on Pt_3Hf_1 substrates than on Pt_1Hf_3 and Pt_2Hf_2 substrates, as shown by the higher energy stability level of Gr@Pt_3Hf_1.

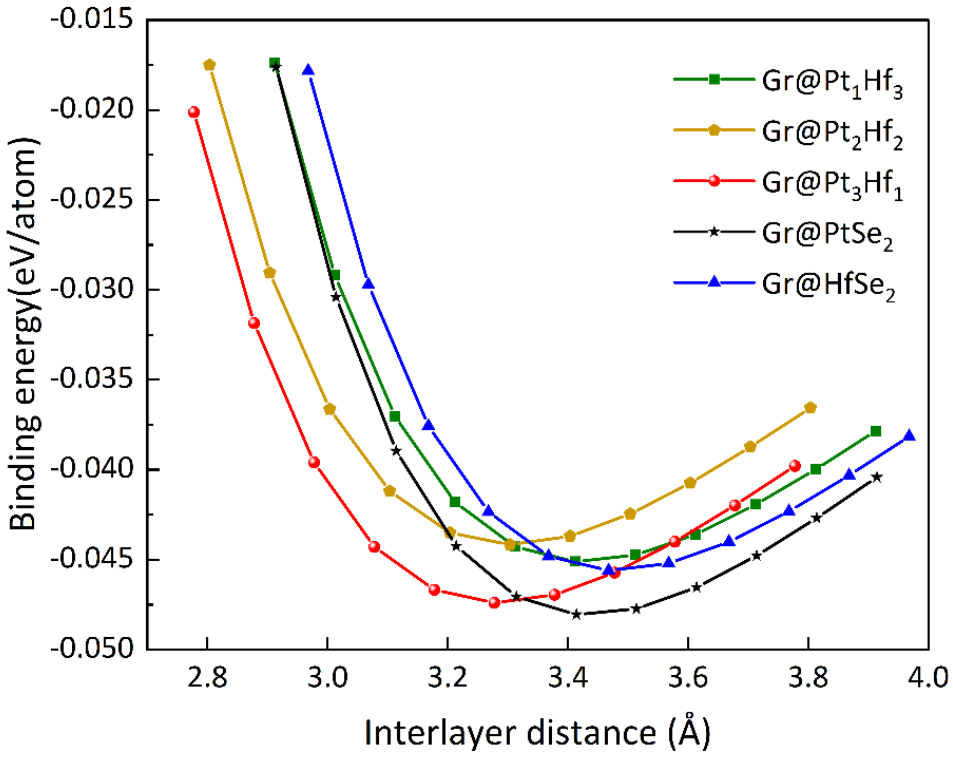

Figure 2. The binding energy of graphene per C atom for Gr@Pt_nHf_{4-n}, as a function of the interlayer distance between graphene and Pt_nHf_{4-n}.

Table 1. The lattice constants (Å), bond lengths (Å) of Pt–Se and Hf–Se, and lattice mismatch ratios of $Gr@Pt_nHf_{4-n}$.

Materials	$Gr@PtSe_2$	$Gr@Pt_1Hf_3$	$Gr@Pt_2Hf_2$	$Gr@Pt_3Hf_1$	$Gr@HfSe_2$
Lattice constants (Å)	a = 12.84 b = 7.41	a = 12.79 b = 7.42	a = 12.78 b = 7.42	a = 12.77 b = 7.41	a = 12.85 b = 7.43
$d_{Pt\text{-}Se}$ (Å), $d_{Hf\text{-}Se}$ (Å)	2.52, -	2.55, 2.67	2.54, 2.67	2.53, 2.63	-, 2.70
Lattice mismatch ratios	0.54%	1.4%	1.4%	1.4%	1.3%

3.2. Electronic Structures of $Gr@Pt_nHf_{4-n}$

The electrical structure of $Gr@Pt_nHf_{4-n}$ is investigated in this section. The overall characteristics of the band structure obtained from the PBE and HSE06 generalization calculations were similar, except that the band gap value obtained from the HSE06 generalization calculations was almost doubled. Additionally, constrained by computing resources, mostly PBE was used in the following computations. The band structures (Figure 3), the total density of states (TDOS), and the projected density of states (PDOS) of monolayer Pt_1Hf_3, Pt_2Hf_2, Pt_3Hf_1, graphene, $PtSe_2$, and $HfSe_2$ were determined (Figure 4). In Figure 3d, the band structure of pristine graphene shows a typical Dirac point located at the point of the Brillouin zone. The projected density of states (PDOS) illuminates that the states of graphene are delocalized around the Fermi level. The band structure of Pt_nHf_{4-n} exhibits semiconductor characteristics.

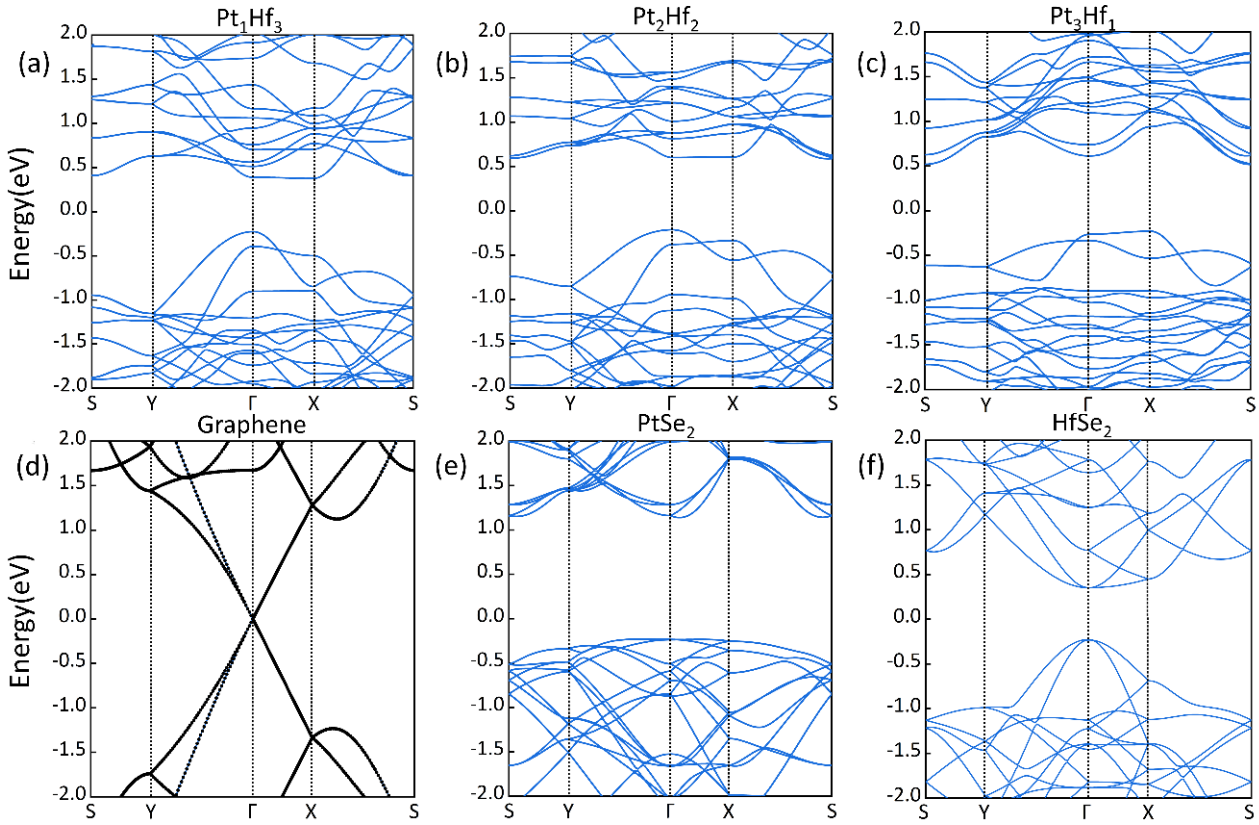

Figure 3. Band structures of monolayers: (**a**) Pt_1Hf_3, (**b**) Pt_2Hf_2, (**c**) Pt_3Hf_1, (**d**) Graphene, (**e**) $PtSe_2$, and (**f**) $HfSe_2$.

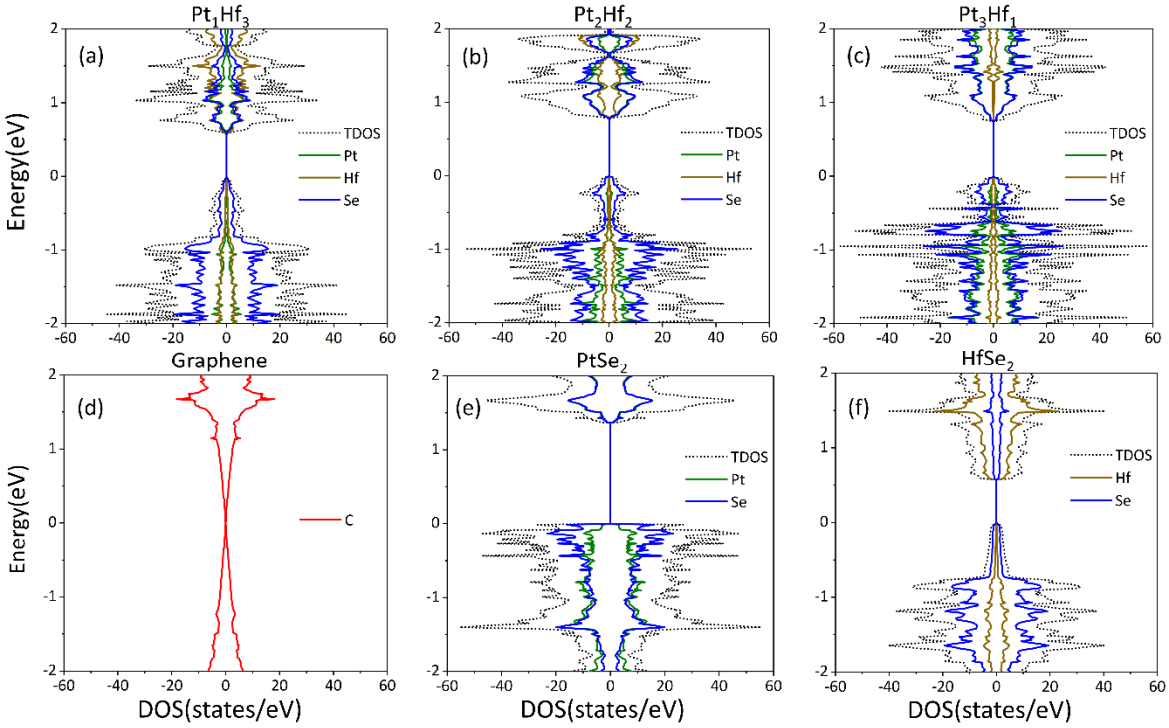

Figure 4. Calculated DOS and PDOS for (**a**) Pt_1Hf_3, (**b**) Pt_2Hf_2, (**c**) Pt_3Hf_1, (**d**) Graphene, (**e**) $PtSe_2$, and (**f**) $HfSe_2$, where an energy level of zero is scaled to the Fermi level.

Next, the projected band structure of the five heterostructures, Gr@Pt_1Hf_3, Gr@Pt_2Hf_2, Gr@Pt_3Hf_1, Gr@$PtSe_2$, and Gr@$HfSe_2$, were calculated. Compared to Figure 3, the band structure of the Gr@Pt_nHf_{4-n} bidirectional heterostructures were almost a superposition of two monolayer bands, indicating that the bidirectional heterostructure preserves the good electronic characteristics of its monolayer material and also extends the enriched properties. As seen in Figure 5, the band gaps of Gr@$PtSe_2$ and Gr@$HfSe_2$ were 0.0203 eV and 0.0853 eV, respectively. This is in broad accord with previously published calculations [28,36]. Band gaps of the combined structure of Gr@Pt_1Hf_3, Gr@Pt_2Hf_2, and Gr@Pt_3Hf_1 were 0.0182 eV, 0.0351 eV, and 0.0397 eV, respectively. According to the calculations, the band gaps of the bidirectional heterostructures, Gr@Pt_1Hf_3, Gr@Pt_2Hf_2, and Gr@Pt_3Hf_1, were all between the band gaps of Gr@$PtSe_2$ and Gr@$HfSe_2$. The results showed that the band gaps of the bidirectional heterostructures grew progressively as the percentage of Pt increased, with Gr@Pt_1Hf_3 and Gr@Pt_2Hf_2 showing an indirect band gap between point Y and point Γ, while Gr@Pt_3Hf_1 exhibited a direct band gap at point Γ.

For the bidirectional heterostructures of Gr@Pt_nHf_{4-n}, with the Bader charge analysis (Table 2), we find the electronic charge transfer from graphene to the top Se atoms when graphene adheres to Se-terminated substrates. A more evident view of the charge redistribution and transfer between the graphene and Pt_nHf_{4-n} polar surface can be obtained by calculating the charge density differences before and after the charge transfer. Such a charge density difference ($\Delta\rho$) can be calculated using the following equation:

$$\Delta\rho(z) = \rho_{Gr@Pt_nHf_{4-n}} - \rho_{Pt_nHf_{4-n}} - \rho_{Gr}, \quad (6)$$

where $\rho Gr@Pt_nHf_{4-n}$, ρPt_nHf_{4-n}, and ρ_{Gr} are the total plane-averaged electron densities of the bidirectional heterostructures of Gr@Pt_nHf_{4-n}, the individual lateral heterostructures of Pt_nHf_{4-n}, and the graphene monolayer, respectively, which are shown in Figure 6. The charge rearrangements following the development of the heterostructures, as seen in Figure 6, indicate that the charge transfers in the five structures are comparable and mostly occur near the interface (interlayer transfer). In these heterostructures, electrons are lost on the graphene side, while they are mostly grouped on the Pt_nHf_{4-n} side, with a tiny amount

clustered on the graphene side. It is found that $\Delta\rho(z) < 0$ near the graphene and $\Delta\rho(z) > 0$ at the top of the Se atoms of the Pt_nHf_{4-n} slab substrate. This implies that the electrons are transferred from the graphene to the Pt_nHf_{4-n} layer, resulting in electron–hole (e–h) separation. A polarized field pointing from the graphene layer to the Pt_nHf_{4-n} substrate is generated. In each of the five configurations, there is a distinct transfer of electrons from graphene to Pt_nHf_{4-n}, but the charge collected on the Pt_nHf_{4-n} differs. In short, as long as the graphene monolayer adheres to the Pt_nHf_{4-n} substrate, electrons will gather in the region near the Pt_nHf_{4-n}, while holes will accumulate on the graphene monolayer, generating e–h pairs.

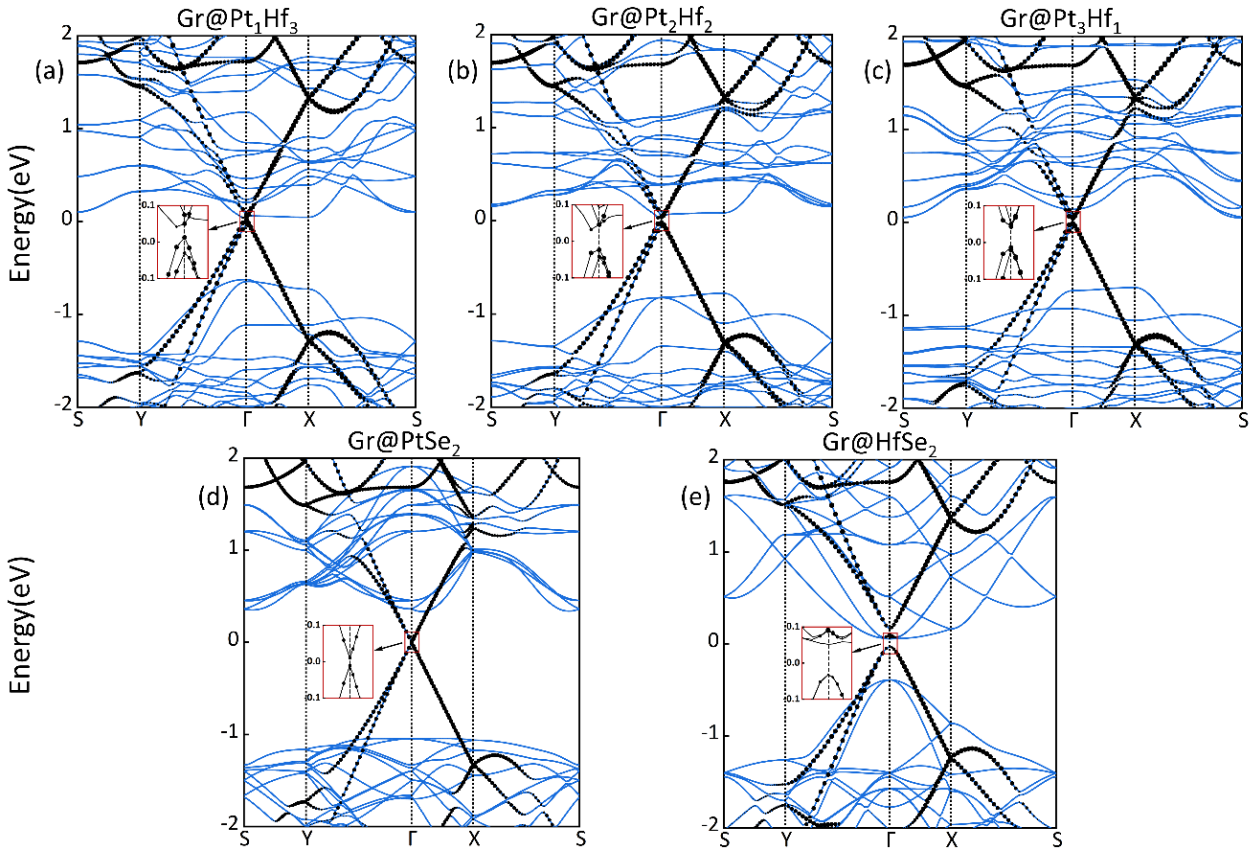

Figure 5. Projected band structures of bidirectional heterostructures of (**a**) $Gr@Pt_1Hf_3$, (**b**) $Gr@Pt_2Hf_2$, and (**c**) $Gr@Pt_3Hf_1$. Projected band structures of (**d**) $Gr@PtSe_2$ and (**e**) $Gr@HfSe_2$.

Table 2. Interfacial distance, *d* (Å), and acquired charges, (*e*), of graphene in the fully optimized configurations of the $Gr@Pt_1Hf_3$, $Gr@Pt_2Hf_2$, $Gr@Pt_3Hf_1$, $Gr@PtSe_2$, and $Gr@HfSe_2$ heterostructures, respectively.

Materials	*d* (Å)	Acquired Charges in Graphene (*e*)
$Gr@Pt_1Hf_3$	3.42	−0.20
$Gr@Pt_2Hf_2$	3.31	−0.26
$Gr@Pt_3Hf_1$	3.27	−0.28
$Gr@PtSe_2$	3.46	−0.32
$Gr@HfSe_2$	3.41	−0.12

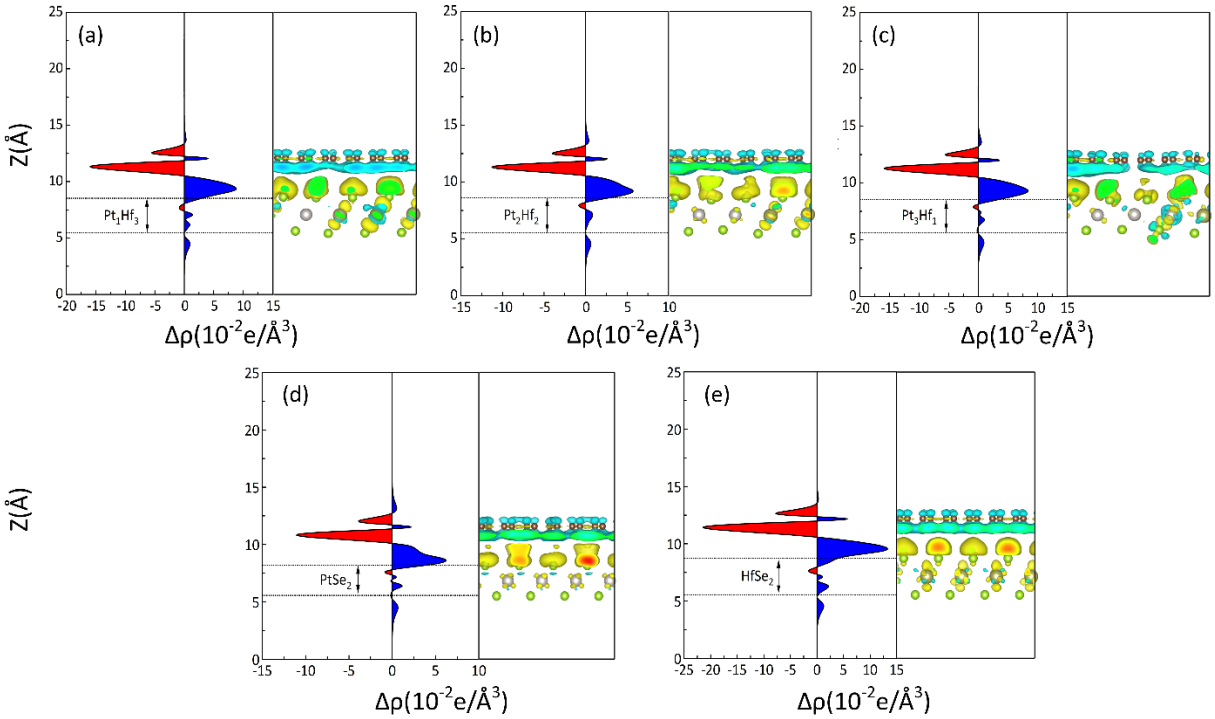

Figure 6. Charge transfer across the interface of the Gr@Pt_nHf_{4-n} heterostructures. On the left is the plane-averaged charge density difference $\Delta\rho(z)$ along the z-direction for the (**a**) Gr@Pt_1Hf_3, (**b**) Gr@Pt_2Hf_2, (**c**) Gr@Pt_3Hf_1, (**d**) Gr@$PtSe_2$, and (**e**) Gr@$HfSe_2$ heterostructures, respectively. The blue and red area represent charge accumulation and depletion, respectively. On the right is side views of the three-dimensional charge density difference plots for corresponding heterostructures, respectively. Yellow and green iso-surfaces represent charge accumulation and depletion in the space with respect to isolated graphene and the Pt_nHf_{4-n} slab substrate.

3.3. Optical Properties of Gr@Pt_nHf_{4-n}

In 2D vdW heterojunctions, it is known that interfacial interaction, charge redistribution, and e–h pair separation are often followed by an enhancement in optical transitions [49]. With the help of e–h pair separation, the light absorption coefficient may increase in the heterostructures. Figure 7 depicts the optical characteristics of the Gr@$PtSe_2$, Gr@$HfSe_2$, and Gr@Pt_nHf_{4-n} heterostructures. Compared to Gr@$PtSe_2$ and Gr@Pt_nHf_{4-n}, Gr@$HfSe_2$ has poor optical absorption properties. Moreover, as the amount of Pt in the Gr@Pt_1Hf_3, Gr@Pt_2Hf_2, and Gr@Pt_3Hf_1 bidirectional heterostructures increases, the peak value of the optical absorption coefficient in the 1.3~40 μm wavelength region rises progressively, particularly in the 0.75~1.33 μm wavelength region, while the peak optical absorption values of Gr@Pt_3Hf_1 and Gr@$PtSe_2$ are similar. The enhanced light absorption may be ascribed to the increased density of Pt and Se states at the bottom of the conduction band. As mentioned before, the holes and electrons of the e–h pairs are located at the graphene monolayer and the Pt_nHf_{4-n} substrate, respectively. Under normal IR light, electrons in the p_z-orbital of graphene are excited to the d-orbitals of the Pt atoms and the p-orbitals of the Se atoms of the conduction band of the Pt_3Hf_1 substrate. In Figure 6, charge redistribution and transfer occur at the top of the Pt_nHf_{4-n} substrate in Gr@Pt_nHf_{4-n}. The charge decreases mostly near the C atoms and subsequently increases at the top of the Se atoms, forming e–h pairs at the interface. Consequently, a polarized field is generated, which guides the orientation of the graphene to the Pt_nHf_{4-n} [50]. It should be noted that the light absorption enhancement of the Gr@Pt_3Hf_1 heterostructure is larger than that of the Gr@Pt_1Hf_3 and Gr@Pt_2Hf_2 heterostructures, and it may also be related to the lower interlayer distance at the surface of the Gr@Pt_3Hf_1 heterostructure. Charge transport is affected by the relatively strong interlayer interaction between the graphene and Pt_3Hf_1 layers. This

indicates that the interaction intensity between the interfaces in a heterostructure may also be an important factor in improving the optical absorption coefficient. We conclude that the interlayer coupling in the bidirectional heterojunction Gr@Pt_nHf_{4-n} is stronger and that the IR light absorption performance is greater with higher Pt concentrations.

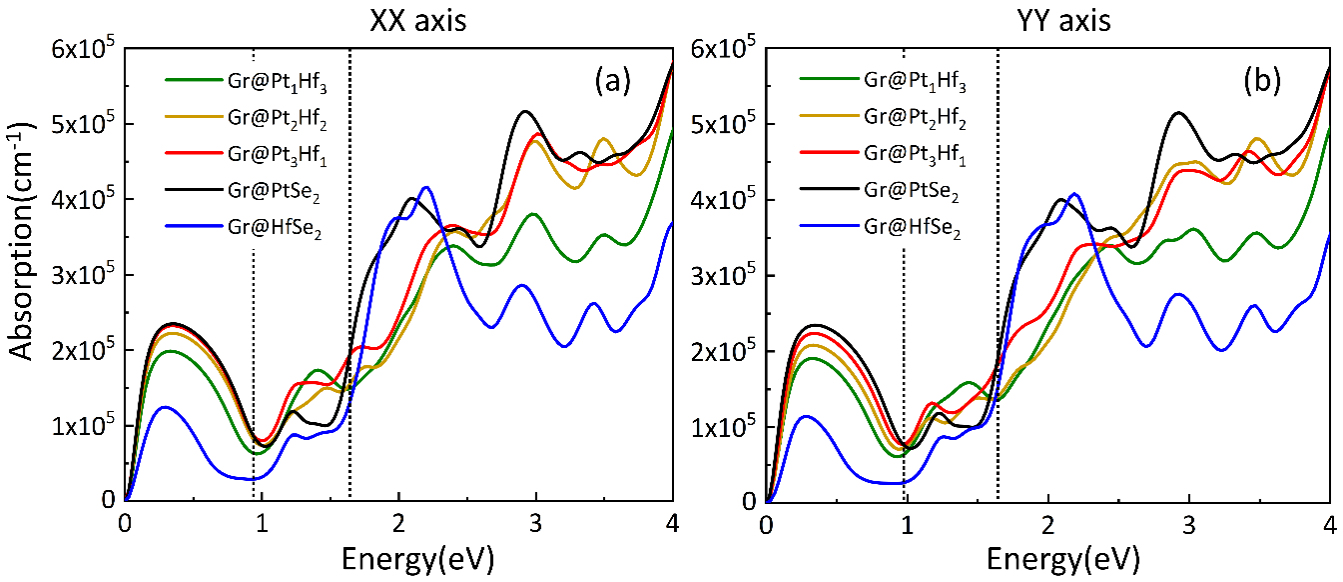

Figure 7. The calculated absorption spectra for the Gr@$PtSe_2$, Gr@Pt_nHf_{4-n}, and Gr@$HfSe_2$ heterostructures are shown in (**a**,**b**) for the XX and YY directions, respectively, where XX represents the long side of the rectangular structure and YY represents the short side of the rectangular structure.

The IR absorption fluctuation patterns of the five heterostructures in the 0.75~1.33 μm IR wavelength region show comparable properties. Combining the band structures of the bidirectional heterostructure of Gr@Pt_nHf_{4-n} (Figure 5a–c), we observed that the reduced band gaps of Gr@Pt_1Hf_3, Gr@Pt_2Hf_2, and Gr@Pt_3Hf_1 will increase their absorption coefficients in the near-infrared to a visible red range relative to Gr@$PtSe_2$. Particularly, in the 1.3~40 μm IR wavelength region, the optical absorption coefficient of Gr@Pt_3Hf_1 is larger than that of Gr@$PtSe_2$ in the near-infrared to visible red-light range (Figure 8). In combination with PDOS (Figure 8c,e), the peak of DOS at 0.6~1.2 eV for Gr@Pt_3Hf_1 is more than that of Gr@$PtSe_2$, and the interval corresponds to the region in which the optical absorption coefficient of Gr@Pt_3Hf_1 is greater than that of Gr@$PtSe_2$. Therefore, we propose that doping Hf atoms may be the reason why the electronic state of Gr@Pt_3Hf_1 is more active, leading to a relatively strong absorption peak in the 1.3~40 μm IR wavelength region of its absorption spectrum. This provides Gr@Pt_3Hf_1 to replace Gr@$PtSe_2$ in the NIR detector, allowing the detection range to be expanded from the NIR to the visible red range. Our findings indicate that the absorptive properties of Gr@Pt_3Hf_1 in the NIR range are almost the same as those of Gr@$PtSe_2$, but the absorptive properties in the 0.75~1.33 μm wavelength region in the NIR are greater than those of Gr@$PtSe_2$. This shows that the bidirectional heterostructure of Gr@Pt_3Hf_1 is a cost-effective design method.

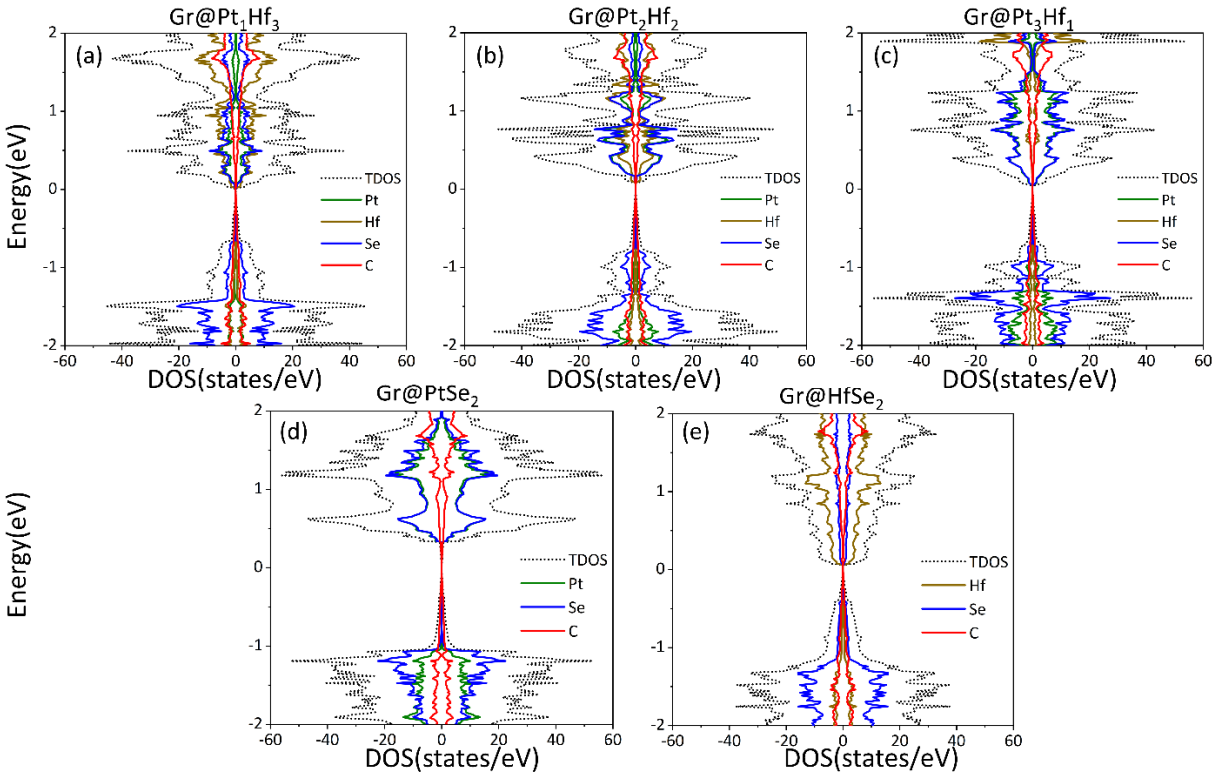

Figure 8. Calculated DOS and PDOS for (**a**) Gr@Pt_1Hf_3, (**b**) Gr@Pt_2Hf_2, (**c**) Gr@Pt_3Hf_1, (**d**) Gr@$PtSe_2$, and (**e**) Gr@$HfSe_2$. An energy level of zero is assigned to the Fermi level.

4. Conclusions

In conclusion, we have analyzed the electrical and optical characteristics of the bidirectional heterostructure of Gr@Pt_nHf_{4-n} using first-principles calculations. It was found that the bidirectional heterostructures of Gr@Pt_nHf_{4-n} had similar band structures, and that the band gap of graphene was opened by Pt_nHf_{4-n} in the presence of an inhomogeneous electrostatic potential generated by Pt_nHf_{4-n}. The charge was transferred from graphene to Pt_nHf_{4-n}, and a polarized field was generated at the interface between graphene and Pt_nHf_{4-n}. As the percentage of Pt in Gr@Pt_nHf_{4-n} increased, the band gaps of Gr@Pt_1Hf_3, Gr@Pt_2Hf_2, and Gr@Pt_3Hf_1 continued to expand, and the infrared light absorption performance also improved. In particular, the optical absorption capacity of the Gr@Pt_3Hf_1 structure was equivalent to that of Gr@$PtSe_2$ in the near-infrared 1.3~40 μm range of wavelength, while it was superior to Gr@$PtSe_2$ in the near-infrared to the visible red-light wavelength band of 0.75~1.33 μm. These theoretical findings imply that the Gr@Pt_3Hf_1 structure is a design method that is equivalent to the Gr@$PtSe_2$ structure in terms of near-infrared detection performance, which may efficiently decrease material costs and expand the near-infrared light detection interval. These findings show that the bidirectional heterostructure of Gr@Pt_3Hf_1 may apply to large-scale infrared photodetectors.

Supplementary Materials: The following supporting information can be downloaded at: https://www.mdpi.com/article/10.3390/cryst12091244/s1, Figure S1: The calculated absorption spectra for the Gr@$PtSe_2$, Gr@Pt_nZr_{4-n} and Gr@$ZrSe_2$ heterostructures; Figure S2: The calculated absorption spectra for the Gr@Pt_nHf_{4-n} and Gr@Pt_nZr_{4-n} heterostructures; Figure S3: The Bravais lattice, Brillouin zone and K- paths for the designed hexagonal and rectangular structures.

Author Contributions: Conceptualization, J.Z.; data curation, J.Z. and J.P.; formal analysis, H.D.; funding acquisition, F.W.; investigation, J.Z. and H.H.; methodology, C.L.; project administration, H.D.; software, J.Z. and S.K.; supervision, H.D. and F.W.; writing—original draft, J.Z.; writing—review and editing, H.H., J.P., H.D., Y.X., R.W., M.W. and F.W. All authors have read and agreed to the published version of the manuscript.

Funding: This research was funded by the Guangdong Natural Science Foundation of China (Grants No. 2017B030306003, and No. 2019B1515120078) and the National Natural Science Foundation of China (Grant No. 11804057).

Institutional Review Board Statement: Not applicable.

Informed Consent Statement: Not applicable.

Data Availability Statement: Not applicable.

Acknowledgments: This work is supported by the Guangdong Natural Science Foundation of China (Grants No. 2017B030306003, and No. 2019B1515120078) and the National Natural Science Foundation of China (Grant No. 11804057). We thank the Center of Campus Network & Modern Educational Technology, Guangdong University of Technology, Guangdong, China for providing computational resources and technical support for this work.

Conflicts of Interest: The authors declare no conflict of interest.

References

1. Xu, X.D.; Yao, W.; Xiao, D.; Heinz, T.F. Spin and pseudospins in layered transition metal dichalcogenides. *Nat. Phys.* **2014**, *10*, 343–350. [CrossRef]
2. Chhowalla, M.; Shin, H.S.; Eda, G.; Li, L.J.; Loh, K.P.; Zhang, H. The chemistry of two-dimensional layered transition metal dichalcogenide nanosheets. *Nat. Chem.* **2013**, *5*, 263–275. [CrossRef] [PubMed]
3. Zeng, H.; Dai, J.; Yao, W.; Xiao, D.; Cui, X. Valley polarization in MoS2 monolayers by optical pumping. *Nat. Nanotechnol.* **2012**, *7*, 490–493. [CrossRef]
4. Mogulkoc, Y.; Modarresi, M.; Mogulkoc, A.; Ciftci, Y.O. Electronic and optical properties of bilayer blue phosphorus. *Comput. Mater. Sci.* **2016**, *124*, 23–29. [CrossRef]
5. Xie, J.F.; Zhang, D.; Yan, X.Q.; Ren, M.X.; Zhao, X.; Liu, F.; Sun, R.X.; Li, X.K.; Li, Z.; Chen, S.Q.; et al. Optical properties of chemical vapor deposition-grown $PtSe_2$ characterized by spectroscopic ellipsometry. *2D Mater.* **2019**, *6*, 035011. [CrossRef]
6. Zhang, K.; Zhang, T.; Cheng, G.; Li, T.; Wang, S.; Wei, W.; Zhou, X.; Yu, W.; Sun, Y.; Wang, P.; et al. Interlayer Transition and Infrared Photodetection in Atomically Thin Type-II MoTe(2)/MoS(2) van der Waals Heterostructures. *ACS Nano* **2016**, *10*, 3852–3858. [CrossRef] [PubMed]
7. Lee, C.-H.; Lee, G.-H.; Van Der Zande, A.M.; Chen, W.; Li, Y.; Han, M.; Cui, X.; Arefe, G.; Nuckolls, C.; Heinz, T.F. Atomically thin p–n junctions with van der Waals heterointerfaces. *Nat. Nanotechnol.* **2014**, *9*, 676–681. [CrossRef] [PubMed]
8. Zeng, L.H.; Lin, S.H.; Li, Z.J.; Zhang, Z.X.; Zhang, T.F.; Xie, C.; Mak, C.H.; Chai, Y.; Lau, S.P.; Luo, L.B.; et al. Fast, Self-Driven, Air-Stable, and Broadband Photodetector Based on Vertically Aligned $PtSe_2$/GaAs Heterojunction. *Adv. Funct. Mater.* **2018**, *28*, 1705970. [CrossRef]
9. Yu, J.H.; Lee, H.R.; Hong, S.S.; Kong, D.; Lee, H.-W.; Wang, H.; Xiong, F.; Wang, S.; Cui, Y. Vertical heterostructure of two-dimensional MoS_2 and WSe_2 with vertically aligned layers. *Nano Lett.* **2015**, *15*, 1031–1035. [CrossRef]
10. Ebnonnasir, A.; Narayanan, B.; Kodambaka, S.; Ciobanu, C.V. Tunable MoS_2 bandgap in MoS_2-graphene heterostructures. *Appl. Phys. Lett.* **2014**, *105*, 031603. [CrossRef]
11. Ju, W.W.; Zhang, Y.; Li, T.W.; Wang, D.H.; Zhao, E.Q.; Hu, G.X.; Xu, Y.M.; Li, H.S. A type-II WSe_2/$HfSe_2$ van der Waals heterostructure with adjustable electronic and optical properties. *Results Phys.* **2021**, *25*, 104250. [CrossRef]
12. Massicotte, M.; Schmidt, P.; Vialla, F.; Schädler, K.G.; Reserbat-Plantey, A.; Watanabe, K.; Taniguchi, T.; Tielrooij, K.-J.; Koppens, F.H. Picosecond photoresponse in van der Waals heterostructures. *Nat. Nanotechnol.* **2016**, *11*, 42–46. [PubMed]
13. Mitra, S.; Banerjee, S.; Datta, A.; Chakravorty, D. A brief review on graphene/inorganic nanostructure composites: Materials for the future. *Indian J. Phys.* **2016**, *90*, 1019–1032.
14. Wu, D.; Wang, Y.E.; Zeng, L.H.; Jia, C.; Wu, E.P.; Xu, T.T.; Shi, Z.F.; Tian, Y.T.; Li, X.J.; Tsang, Y.H. Design of 2D Layered $PtSe_2$ Heterojunction for the High-Performance, Room-Temperature, Broadband, Infrared Photodetector. *ACS Photonics* **2018**, *5*, 3820–3827.
15. Wang, Y.; Li, L.; Yao, W.; Song, S.; Sun, J.T.; Pan, J.; Ren, X.; Li, C.; Okunishi, E.; Wang, Y.Q.; et al. Monolayer PtSe(2), a New Semiconducting Transition-Metal-Dichalcogenide, Epitaxially Grown by Direct Selenization of Pt. *Nano Lett.* **2015**, *15*, 4013–4018. [PubMed]
16. Novoselov, K.S.; Geim, A.K.; Morozov, S.V.; Jiang, D.-E.; Zhang, Y.; Dubonos, S.V.; Grigorieva, I.V.; Firsov, A.A. Electric field effect in atomically thin carbon films. *Science* **2004**, *306*, 666–669. [CrossRef]
17. Kumar, N.; Sharma, M.; Sharma, J.; Ahluwalia, P. Study of magnetism in nano structures of graphene and functionalized graphene: A first principle study. *Indian J. Phys.* **2015**, *89*, 143–150. [CrossRef]
18. Zhao, B.; Zhao, J.; Zhang, Z. Resonance enhanced absorption in a graphene monolayer using deep metal gratings. *JOSA B* **2015**, *32*, 1176–1185. [CrossRef]
19. Lu, Y.; Song, J.; Yuan, J.; Zhang, L.; Wu, S.Q.Y.; Yu, W.; Zhao, M.; Qiu, C.-W.; Teng, J.; Loh, K.P. Highly efficient plasmon excitation in graphene-Bi_2Te_3 heterostructure. *JOSA B* **2016**, *33*, 1842–1846. [CrossRef]

20. Amin, R.; Ma, Z.; Maiti, R.; Khan, S.; Khurgin, J.B.; Dalir, H.; Sorger, V.J. Attojoule-efficient graphene optical modulators. *Appl. Opt.* **2018**, *57*, D130–D140.
21. Hajati, Y.; Zanbouri, Z.; Sabaeian, M. Optimizing encapsulated graphene in hexagonal boron nitride toward low propagation loss and enhanced field confinement. *JOSA B* **2019**, *36*, 1189–1199.
22. Al-Ashi, N.E.; Taya, S.A.; El-Naggar, S.A.; Vigneswaran, D.; Amiri, I. Optical fiber surrounded by a graphene layer as an optical sensor. *Opt. Quantum Electron.* **2020**, *52*, 1–10.
23. Ojaghi, S.; Golmohammadi, S.; Soofi, H. All-optical graphene-on-silicon slot waveguide modulator based on graphene's Kerr effect. *Appl. Opt.* **2021**, *60*, 7945–7954.
24. Daher, M.G.; Taya, S.A.; Colak, I.; Patel, S.K.; Olaimat, M.M.; Ramahi, O. Surface plasmon resonance biosensor based on graphene layer for the detection of waterborne bacteria. *J. Biophotonics* **2022**, *15*, e202200001. [PubMed]
25. Yupapin, P.; Trabelsi, Y.; Vigneswaran, D.; Taya, S.A.; Daher, M.G.; Colak, I. Ultra-High-Sensitive Sensor Based on Surface Plasmon Resonance Structure Having Si and Graphene Layers for the Detection of Chikungunya Virus. *Plasmonics* **2022**, *17*, 1315–1321.
26. Kashuba, A.B. Conductivity of defectless graphene. *Phys. Rev. B* **2008**, *78*, 085415.
27. Tan, Y.-W.; Zhang, Y.; Bolotin, K.; Zhao, Y.; Adam, S.; Hwang, E.; Sarma, S.D.; Stormer, H.; Kim, P. Measurement of scattering rate and minimum conductivity in graphene. *Phys. Rev. Lett.* **2007**, *99*, 246803.
28. Guan, Z.Y.; Ni, S.; Hu, S.L. Band gap opening of graphene by forming a graphene/$PtSe_2$ van der Waals heterojunction. *Rsc. Adv.* **2017**, *7*, 45393–45399.
29. Long, M.S.; Liu, F.K.; Ding, F.; Wang, Y.; Ye, J.F.; Xie, R.Z.; Wang, H.; Xu, M.J.; Wang, F.; Tu, Y.B.; et al. Scalable fabrication of long-wave infrared $PtSe_2$-G heterostructure array photodetectors. *Appl. Phys. Lett.* **2020**, *117*, 231104.
30. Wang, L.; Li, J.J.; Fan, Q.; Huang, Z.F.; Lu, Y.C.; Xie, C.; Wu, C.Y.; Luo, L.B. A high-performance near-infrared light photovoltaic detector based on a multilayered $PtSe_2$/Ge heterojunction. *J. Mater. Chem. C* **2019**, *7*, 5019–5027.
31. Zeng, L.H.; Lin, S.H.; Lou, Z.H.; Yuan, H.Y.; Long, H.; Li, Y.Y.; Lu, W.; Lau, S.P.; Wu, D.; Tsang, Y.H. Ultrafast and sensitive photodetector based on a $PtSe_2$/silicon nanowire array heterojunction with a multiband spectral response from 200 to 1550 nm. *NPG Asia Mater.* **2018**, *10*, 352–362.
32. Zhang, X.; Gao, Y. 2D/2D h-BN/N-doped MoS_2 Heterostructure Catalyst with Enhanced Peroxidase-like Performance for Visual Colorimetric Determination of H_2O_2. *Chem. -Asian J.* **2020**, *15*, 1315–1323. [PubMed]
33. Wei, L.Y.; Lian, C.; Meng, S. Prediction of two-dimensional electron gas mediated magnetoelectric coupling at ferroelectric $PbTiO_3$/$SrTiO_3$ heterostructures. *Phys. Rev. B* **2017**, *95*, 184102.
34. Yue, R.; Barton, A.T.; Zhu, H.; Azcatl, A.; Pena, L.F.; Wang, J.; Peng, X.; Lu, N.; Cheng, L.; Addou, R.; et al. $HfSe_2$ thin films: 2D transition metal dichalcogenides grown by molecular beam epitaxy. *ACS Nano* **2015**, *9*, 474–480. [PubMed]
35. Yin, L.; Xu, K.; Wen, Y.; Wang, Z.X.; Huang, Y.; Wang, F.; Shifa, T.A.; Cheng, R.; Ma, H.; He, J. Ultrafast and ultrasensitive phototransistors based on few-layered $HfSe_2$. *Appl. Phys. Lett.* **2016**, *109*, 213105. [CrossRef]
36. Luo, Q.; Yin, S.; Sun, X.; Guo, G.; Dai, X. Interlayer coupling and external electric field controllable electronic structures and Schottky contact of HfSeX (X = S, Se)/graphene van der Waals heterostructures. *Diam. Relat. Mater.* **2022**, *128*, 109223.
37. Zhao, Q.Y.; Guo, Y.H.; Si, K.Y.; Ren, Z.Y.; Bai, J.T.; Xu, X.L. Elastic, electronic, and dielectric properties of bulk and monolayer ZrS_2, $ZrSe_2$, HfS_2, $HfSe_2$ from van der Waals density-functional theory. *Phys. Status Solidi B* **2017**, *254*, 1700033.
38. Kresse, G.; Furthmüller, J. Efficiency of ab-initio total energy calculations for metals and semiconductors using a plane-wave basis set. *Comp. Mater. Sci.* **1996**, *6*, 15–50.
39. Kresse, G.; Furthmüller, J. Efficient iterative schemes for ab initio total-energy calculations using a plane-wave basis set. *Phys. Rev. B* **1996**, *54*, 11169.
40. Perdew, J.P.; Burke, K.; Ernzerhof, M. Generalized gradient approximation made simple. *Phys. Rev. Lett.* **1996**, *77*, 3865.
41. Grimme, S.; Antony, J.; Ehrlich, S.; Krieg, H. A consistent and accurate ab initio parametrization of density functional dispersion correction (DFT-D) for the 94 elements H-Pu. *J. Chem. Phys.* **2010**, *132*, 154104. [PubMed]
42. Grimme, S.; Ehrlich, S.; Goerigk, L. Effect of the damping function in dispersion corrected density functional theory. *J. Comput. Chem.* **2011**, *32*, 1456–1465. [PubMed]
43. Gajdoš, M.; Hummer, K.; Kresse, G.; Furthmüller, J.; Bechstedt, F. Linear optical properties in the projector-augmented wave methodology. *Phys. Rev. B* **2006**, *73*, 045112. [CrossRef]
44. Eberlein, T.; Bangert, U.; Nair, R.; Jones, R.; Gass, M.; Bleloch, A.; Novoselov, K.; Geim, A.; Briddon, P. Plasmon spectroscopy of free-standing graphene films. *Phys. Rev. B* **2008**, *77*, 233406.
45. Wang, V.; Xu, N.; Liu, J.C.; Tang, G.; Geng, W.T. VASPKIT: A user-friendly interface facilitating high-throughput computing and analysis using VASP code. *Comput. Phys. Commun.* **2021**, *267*, 108033.
46. Wang, J.; Zhao, X.; Hu, G.; Ren, J.; Yuan, X. Manipulable Electronic and Optical Properties of Two-Dimensional MoSTe/$MoGe_2N_4$ van der Waals Heterostructures. *Nanomaterials* **2021**, *11*, 3338. [PubMed]
47. Setiyawati, I.; Chiang, K.R.; Ho, H.M.; Tang, Y.H. Distinct electronic and transport properties between 1T-$HfSe_2$ and 1T-$PtSe_2$. *Chin. J. Phys.* **2019**, *62*, 151–160.
48. Liou, S.; Shie, C.-S.; Chen, C.; Breitwieser, R.; Pai, W.; Guo, G.; Chu, M.-W. π-plasmon dispersion in free-standing graphene by momentum-resolved electron energy-loss spectroscopy. *Phys. Rev. B* **2015**, *91*, 045418. [CrossRef]

49. Du, A.; Sanvito, S.; Li, Z.; Wang, D.; Jiao, Y.; Liao, T.; Sun, Q.; Ng, Y.H.; Zhu, Z.; Amal, R.; et al. Hybrid graphene and graphitic carbon nitride nanocomposite: Gap opening, electron-hole puddle, interfacial charge transfer, and enhanced visible light response. *J. Am. Chem. Soc.* **2012**, *134*, 4393–4397.
50. Ning, F.; Wang, D.; Feng, Y.X.; Tang, L.M.; Zhang, Y.; Chen, K.Q. Strong interfacial interaction and enhanced optical absorption in graphene/InAs and MoS_2/InAs heterostructures. *J. Mater. Chem. C* **2017**, *5*, 9429–9438.